J Mater Sci: Mater Electron (2021) 32:12094–12110

W- and Mo-based polyoxometalates (POM) as interlayer in Al/*n*–Si photodiodes

Esma Yenel[1,2,*], Yasemin Torlak[3], Adem Kocyigit[4,5], İbrahim Erden[2], Mahmut Kuş[6], and Murat Yıldırım[7,*]

[1] School of Technical Science, Department of Electricity and Energy, Konya Technical University, Konya, Turkey
[2] Department of Chemistry, Yıldız Technical University, İstanbul, Turkey
[3] Cal Vocational High School, Pamukkale University, Denizli, Turkey
[4] Department of Electrical Electronic Engineering, Engineering Faculty, Igdir University, Igdir, Turkey
[5] Department of Electronics and Automation, Vocational High School, Bilecik Şeyh Edebali University, Bilecik, Turkey
[6] Department of Chemical Engineering, Konya Technical University, Konya, Turkey
[7] Department of Biotechnology, Faculty of Science, Selcuk University, Konya, Turkey

Received: 30 January 2021
Accepted: 24 March 2021
Published online: 7 April 2021

ABSTRACT

W- and Mo-based POM layers were fabricated by a chemical method successfully. The FT-IR and NMR spectrometer were performed to obtain structural behaviors of the W- and Mo-based POMs. SEM and AFM image used to reveal the surface morphologies of the W- and Mo-based POMs. The pinhole and crack-free porous surfaces were obtained. Electrochemical behaviors of the W- and Mo-based POMs were studied a galvanostat. Then, the W- and Mo-based POM layers used as film layer between the Al and *n*-Si layer to obtain POM interlayered photodiodes Thus, the Al/*n*–Si (reference), Al/WPOM/*n*–Si and Al/MoPOM/*n*–Si photodiodes were fabricated by evaporating of the metallic and ohmic contact in a thermal evaporator. *I*–*V* measurements were performed on the photodiodes under dark and various light illumination intensities. The photodiodes exhibited good rectifying properties, but rectifying behavior decreased with POM interlayers and increasing light power intensity. The reverse currents of the Al/*n*–Si photodiode increased almost 1000 times at 100 mW/cm^2. However, they increased almost 100 times for the Al/WPOM/*n*–Si and Al/MoPOM/*n*–Si photodiodes. Whereas the forward currents did not change for Al/*n*–Si photodiode, they increased with increasing light power in the case of Al/WPOM/*n*–Si and Al/MoPOM/*n*–Si photodiodes. Various diode parameters such as ideality factor, barrier height and series resistance values were calculated by various techniques and discussed in details. The detector parameters such as responsivity, photosensitivity and specific detectivity values were accounted and compared for the Al/*n*–Si, Al/WPOM/*n*–Si and Al/MoPOM/*n*–Si photodiodes with increasing light power. The POM interlayered photodiodes and photodetectors can be improved for industrial applications.

Address correspondence to E-mail: esmayenel@gmail.com; muratyildirim@selcuk.edu.tr

https://doi.org/10.1007/s10854-021-05838-1

1 Introduction

Recently, polyoxometalates (POMs) have been gained great interest due to their easy synthesis, solubility, excellent electrochemical, optical properties and applications in many fields such as catalyst, molecular electronics and biomedical [1–10]. In addition, thermal and photostability of POMs make them unique materials for molecular electronics [11]. POMs are metal oxide nanoclusters comprising early transition metals such as V, Mo and W in high oxidation states [12]. Although POMs have six different structures defining Keggin, Dawson, Anderson, Waugh, Silverton, and Lindqvist types, but the most widely used structures in applications are Keggin (x/m = 1/12) and Dawson (x/m = 2/18)-type structures [13–17]. Recently our group also investigated the performance of some POM derivatives in organic light emitting diodes, solar cells and thin film transistors. Water soluble lacunary POMs showed excellent electron mobilities in organic light emitting diodes [18]. Performance improvement was also observed in polymer and inverted solar cells using POMs as interlayer materials [19, 20]. We also observed excellent contribution of POMs to performance improvement in thin film transistors [21].

Metal semiconductor devices are obtained contact of a metal and semiconductor for various applications [22, 23]. Sometimes various materials such as insulator, polymers and metal oxides can be inserted between the metal and semiconductor devices to improve electrical properties [24–26]. The metal semiconductor devices can be used as diode, photodiode and photodetector applications instead of p-n junctions [27]. POM layers can be used as interfacial layer between metal and semiconductor to photodiode parameters due to having well lifetime of electrons.

Although many applications of POMs can be available in literature, we have not reached any paper on Schottky diode and photodiode applications of POMs. In this work, the W-doped POM and Mo-doped POM materials were successfully obtained for interlayer of the Schottky diodes. The electrical characteristics of a serial of POM derivatives for photodiode applications by inserting POMs as interlayer between the Al metal and n-Si were investigated. The aim is to obtain more powerful photodiodes by new type of interlayer materials. I–V measurements were employed to obtain electrical characteristics under dark and various light illumination intensities.

2 Experimental

2.1 Materials

All chemicals ($Na_2WO_4{\cdot}2H_2O$, $Na_2MoO_4{\cdot}2H_2O$, Bu_4NBF_4, H_3PO_4, CH_3COOH and KCl) and reagents were commercially purchased from Sigma-Aldrich and used as directly. As a semiconductor material, a (111) oriented n-type Si wafer was employed as substrate from Wafer World. The 99.999% aluminum supplied form Angstrom Science was used as metallic and ohmic contact materials.

2.2 Synthesis of POM compounds

2.2.1 Preparation of α-$K_{7-x}Na_xPW_{11}O_{39}{\cdot}14H_2O$ (WPOM)

45.38 g of $Na_2WO_4{\cdot}2H_2O$ was dissolved in 75 mL ultrapure water and 12.5 mL of H_3PO_4, and then 22 mL of CH_3COOH (glacial) were added dropwise onto this mixture. After the solution was boiled under reflux, 15 g of KCl was added. After - adding the KCI, a white precipitate was formed at the bottom of the solution. This precipitate part was washed with water thoroughly to remove impurities, and then product was dried to obtain WPOM with 58% yield. Detailed synthesize route is available in literature [28].

2.2.2 Preparation of α-$K_9PMo_9O_{34}{\cdot}16H_2O$ (MoPOM)

90.75 g of $Na_2MoO_4{\cdot}2H_2O$ was dissolved in 150 mL ultrapure water and 25 mL of H_3PO_4, and then a 44 mL of CH_3COOH (glacial) was added dropwise onto this mixture. After the solution was boiled under reflux, 30 g of KCl was added. After - adding the KCI, a white precipitate was formed at the bottom of the solution. This precipitate part was washed with water thoroughly to remove impurities, and then product was dried to obtain MoPOM with 58% yield. The synthetization route is also available in literature [28].

2.3 Characterization of Keggin type POMs

The synthesized POMs were characterized structurally by NMR and FT-IR spectrum. ^{31}P NMR spectra were recorded by a Varian ASW-400 (121.49 MHz) spectrometer at room temperature with $(CD_3)_2CO$ and D_2O solutions. IR spectra were obtained as KBr pellets on a Bruker Vertex 70 FT-IR spectrophotometer from 400 to 2000 cm^{-1} wavenumbers. For the further characterization of POM films, surface morphologies were studied using a Zeiss (EVOLS10) model Scanning Electron Microscopy (SEM) and NT-MDT Ntegra model AFM. The electrochemical characterization of the POMs was obtained by Ivium Compactstat model potentiostat/galvanostat with cyclic voltammogram measurements.

2.4 Fabrication and characterization of reference and POM interlayered photodiodes

An *n*-type Si wafer was cut to 2 cm^2 pieces and cleaned in acetone and propanol by an ultrasonic cleaner. HF:H_2O (1:1) solution was used to remove oxide layer from the surface of the wafer pieces, and they immediately transferred to the thermal evaporator to evaporate Al ohmic contact as 100 nm to the back surface of the pieces. Then, they were annealed in N_2 atmosphere at 500 °C for 5 min. POM solutions were deposited on the front surface of the pieces by a spin coater at 3000 rpm for 30 s. 100 nm Au metal layers were covered on the POMs film surfaces as metallic contact by a 1 mm hole array mask. Three different devices were fabricated and named Al/*n*–Si (reference), Al/WPOM/*n*–Si and Al/MoPOM/*n*–Si photodiodes. The schematic diagram of the fabricated photodiodes under light has been illustrated in Fig. 1. Fytronix FY-7000 was used to obtain *I–V* measurements under dark and various illumination conditions from 20 to 100 mW/cm^2 by 20 mW/cm^2 interval. Various devices with CdO and ZnO interfacial layers have been studied for same device geometry [29, 30].

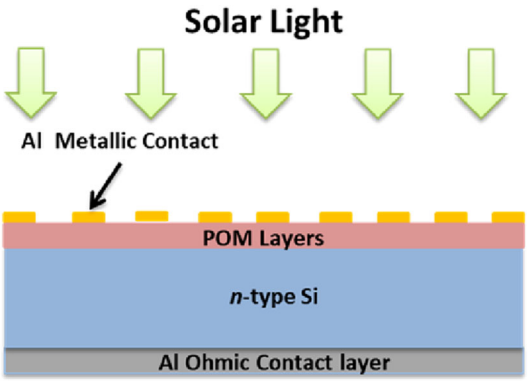

Fig. 1 Schematic illustration of the POM photodiodes under solar simulator

3 Results and discussion

3.1 Structural characterization

Figure 2a and b present the FT-IR spectra of the WPOM and MoPOM structures. The obtained FT-IR spectra for WPOM and MoPOM are compatible with the data in the literature. FT-IR analysis showed two bands at 1086 and 1043 cm^{-1} for WPOM and, 1058 and 1013 cm^{-1} for 1100 and 1034 cm^{-1} for MoPOM assigned to the P–O_i stretching modes of the central PO_4 tetrahedron. The peaks at 1026, 979, 912 cm^{-1} is assigned to (W=O) vibrations. Additionally, the peaks observed at 892, 819, 738 cm^{-1} for WPOM, and 821,744 cm^{-1} for (Mo–O–Mo), and 864, 835, 727 for MoPOM are due to W–O–W vibrations. The vibration bonds have been listed in Table 1 for various the peak values. When the FT-IR spectra are examined, it is seen that the POM framework shifts to the stretching vibration bands towards higher energy depending on the saturation state [31–33].

POMs have characteristic oxygen-to-metal (O → M) ligand-to-metal charge transfer band values in the 900–700 cm^{-1} range [34]. These band values belong to the d-d transitions and inter-valence charge transfer. The charge transfer of the O → M ligand to the metal in this process is similar to the electronic bandgap excitation that occurs in semiconductors. The low energy oxygen 2p orbitals of the POM are similar to the semiconductor valence band and metal d orbitals to the semiconductor conduction band. With the effect of the M–O–M bond in the structure of the POM compounds, the decreases occur consecutively to reduce the absorbance of the O → M ligand-to-metal charge transfer band. In the reduction

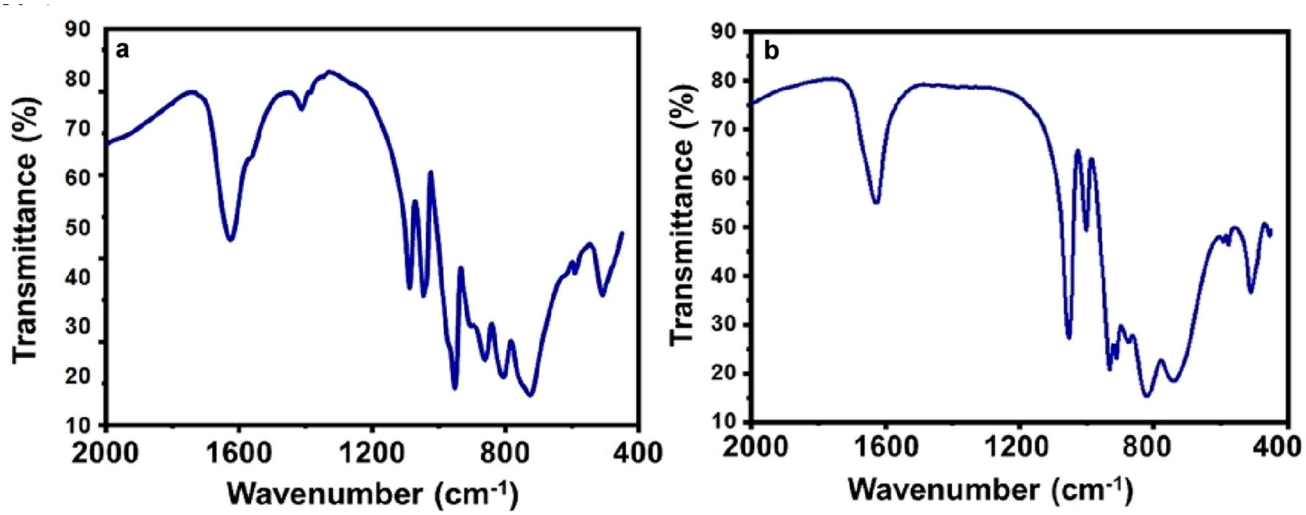

Fig. 2 The IR spectrum of **a** WPOM and **b** MoPOM

Table 1 FT-IR absorptions of WPOM and MoPOM compounds (M–O vibrations observed in the 700–1100 cm^{-1} region)

Compound code	ν_{as} (P–O_i)	ν_{as} (M–O_t)	ν_{as} (M–O–M)
WPOM	1086, 1043	952	903, 860, 806, 728
MoPOM	1058, 1013	934	914, 881, 821, 744

process, the electrons are accepted by the addenda atoms ($W^{VI} \rightarrow W^{V}$). Organic/polymeric materials and carbon-based materials can be joined directly by covalent bonding due to the M–O–M bonds of POM compounds without the need for organic linking groups [35]. The reduced POMs can be studied in various electronic applications [36–38].

^{31}P NMR is used very often to characterize slightly structural changes such as substitution occurring in the framework of phospho-polyoxometalates [39, 40]. ^{31}P NMR spectra of MoPOM in CD_3CN and WPOM in D_2O have been shown in Fig. 3a and b. ^{31}P NMR measurements were collected for the structural analysis of MoPOM in CD_3CN solution and WPOM in D_2O solution. The ^{31}P NMR spectrum of MoPOM has a resonance at $\delta = -15.85$, shifted to low frequency in agreement with the saturation of the framework. When these values in the spectrum are compared, it is seen that the grafting of silane group on structure is not significantly affected by the organic–inorganic backbone group which preserves its trifold symmetry [41–43].

^{31}P-NMR is a useful tool for structural analysis of phosphopolyoxometalates and shows chemical shift in Keggin polyoxsoanions. Obtained anions showed six different chemical shifts for WPOM and MoPOM depending on W–O–W and Mo–O–Mo bonds formations, respectively. ^{31}P NMR of WPOM and MoPOM in D_2O show shifts at $\delta = -11.04$ ppm and $\delta = -12.90$ ppm which corresponds to WPOM and MoPOM structures.

3.2 Morphological characterization of POM compounds

Scanning electron microscopy (SEM) and atomic force microscopy (AFM) was used to characterize the surface morphologies of POM compounds. Figure 4a and b show the SEM images of particle size distributions for WPOM and MoPOM derivatives obtained by 500.00 kX magnifications, respectively. The WPOM appears to be more granular and porous while MoPOM is more complete due to the presence of silane groups in the structure. The porous structure of POMs provides large-specific surface areas. This granular and porous structure both increases the surface area and facilitates electron transfer for electronic device applications [31, 44]. Some of the researchers have used porous structures to obtain more powerful and efficient photodiodes according to literature [45, 46].

Figure 4c, e and d, f show the AFM images WPOM and MoPOM structures on Si surface. As observed in SEM images, similar characteristics are observed in AFM images. WPOM films show smooth surface in comparison with MoPOM films. It can be evaluated

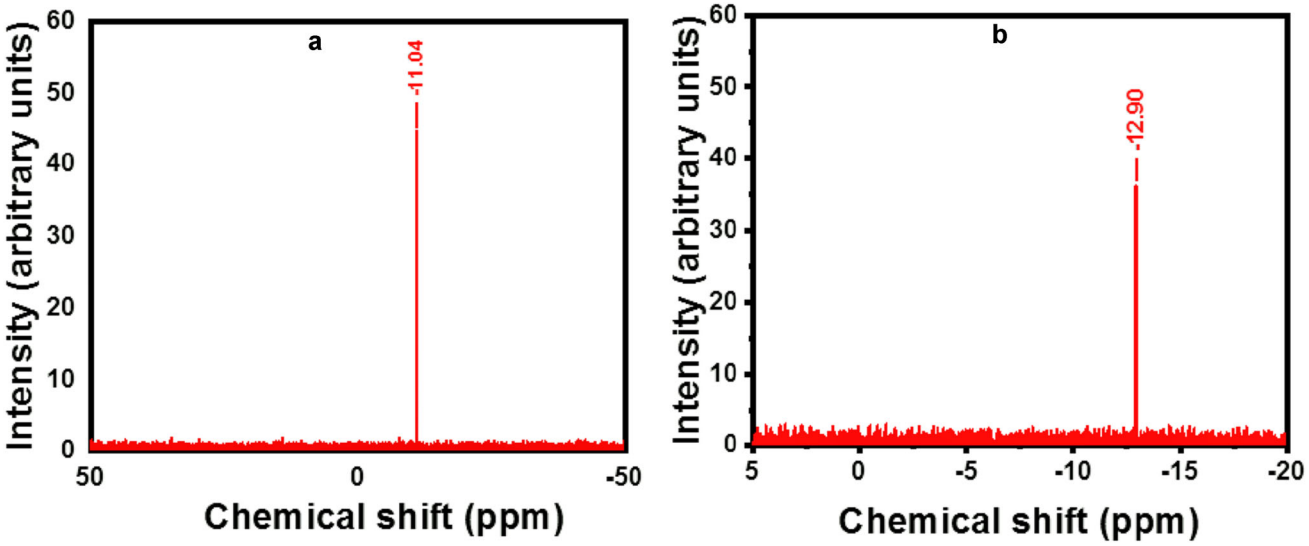

Fig. 3 The ^{31}P NMR spectrum (121.49 MHz, D_2O) of **a** WPOM and **b** MoPOM

to be advantage not to observe any pin holes and micro cracks on films while both films show porous surfaces. AFM and SEM images show that WPOM and MoPOM gives quite smoot and pin hole-free structures by spin coating and this feature is an advantage for thin film device applications. The RMS values of the WPOM and MoPOM were obtained as 2.186 nm and 3.753 nm, respectively.

3.3 Electrochemical properties of POM compounds

Electrochemical behavior of POMs was investigated in a potential range of − 2.0 V to 0 V by cyclic voltammetry technique. While a glassy carbon electrode in acetonitrile was used as transducer and Bu_4NBF_4 was employed as the supporting electrolyte. Figure 5a and b display the cyclic voltammogram graphs of the WPOM and MoPOM, respectively. When the characteristic voltammograms of the WPOM and MoPOM were examined, the redox behavior of tungsten was observed. [31]. In the reduction process, the electrons are accepted by the addenda atoms (W^{VI} and Mo^{VI}). In the potential range between − 2.0 and 0.0 V, the voltammogram curves exhibit redox waves which demonstrate reduction processes for PW_{11} (W^{VI} atoms) and PMo_{11} (Mo^{VI} atoms). In the CV curves of POM (Fig. 5a, b), the pair of peaks at − 0.136 V (E_{ox1})/− 0.541 V (E_{red1}) for WPOM and − 0.362 V (E_{ox1})/− 0.209 V (E_{red1}) for MoPOM were assigned to the oxidation and reduction of the W centers within PW_{11} ($W^{VI} \leftrightarrow W^{V}$). The cyclic voltammetry data and LUMO energy levels of WPOM, and MOPOM compounds are listed in Table 2. We deduced the energy diagram of the junction (Fig. 5c, d), where the LUMO is localized at ΦPOM above the silicon Fermi energy at 4.2 eV below the vacuum level. A similar proposal has been proposed by Laurans et al. [47].

3.4 Electrical characterization of the Al/WPOM/*n*–Si and Al/MoPOM/*n*–Si photodiodes

Electrical characteristics of the Al/*n*–Si (reference), Al/WPOM/*n*–Si and Al/MoPOM/*n*–Si photodiodes were obtained by *I*–*V* measurements. Figure 6a–c display the *I*–*V* characteristics of the Al/*n*–Si, Al/WPOM/*n*–Si and Al/MoPOM/*n*–Si photodiodes under dark and various light power illumination intensities. All three devices have good photodiode behavior because the illumination causes the increasing of the current at reverse as well as zero bias voltage. In the case of Al/*n*–Si reference photodiode, there is no almost increase at forward biases. However, there is distinguishable increase for the Al/WPOM/*n*–Si and Al/MoPOM/*n*–Si photodiodes. This can be attributed to that the W- and Mo-based interfacial POM layers have good response to the illuminations due to decreasing barrier between the Au and *n*-Si and increasing life time of electrons [48]. This result confirms the good and developable behaviors of the POM-based photodiodes or photodetectors [49].

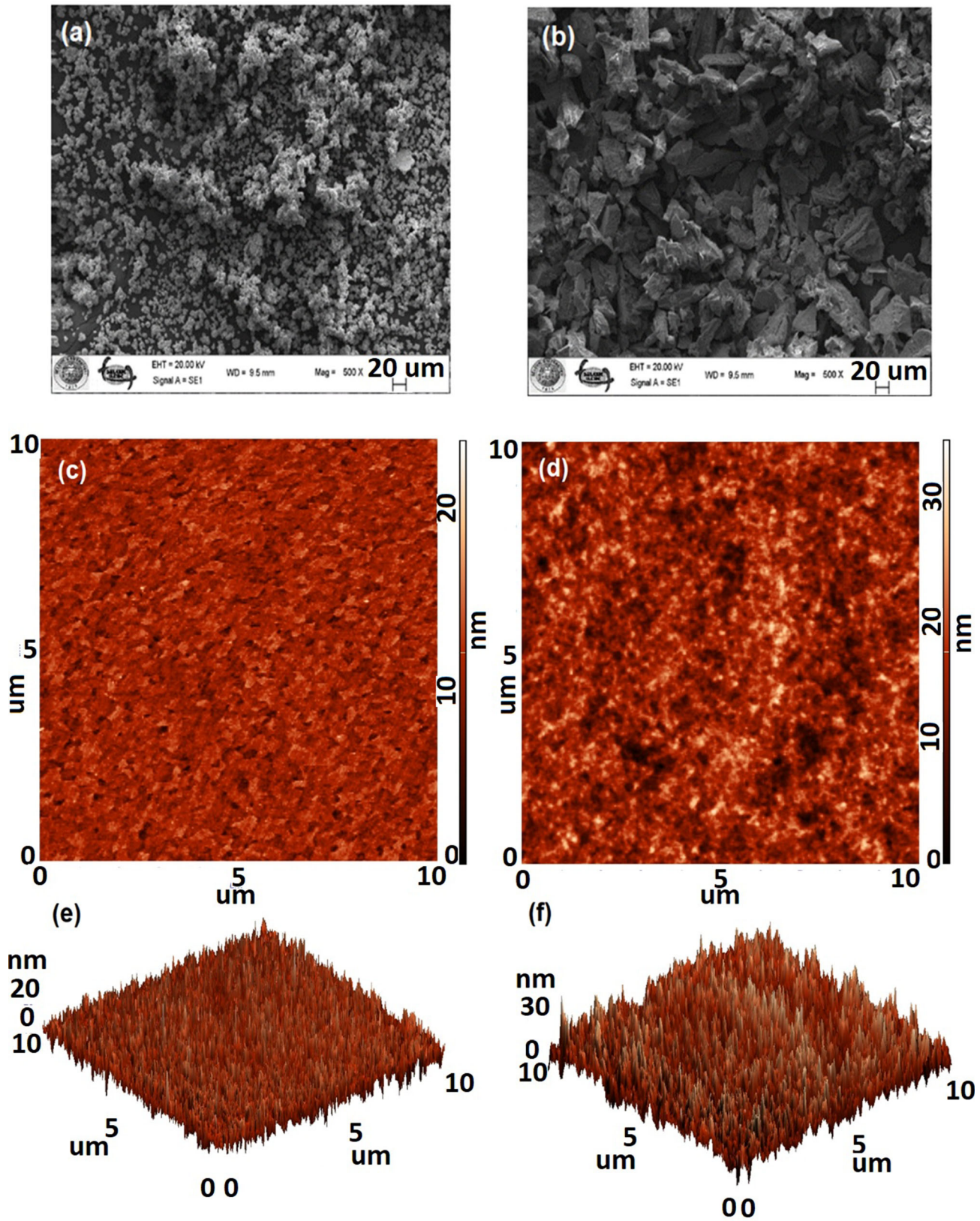

Fig. 4 **a**, **b** SEM (500.00 kX magnification), **c**, **d** 2D and **e**, **f** 3D AFM (40 µm × 40 µm) images of WPOM and MoPOM on ITO, respectively

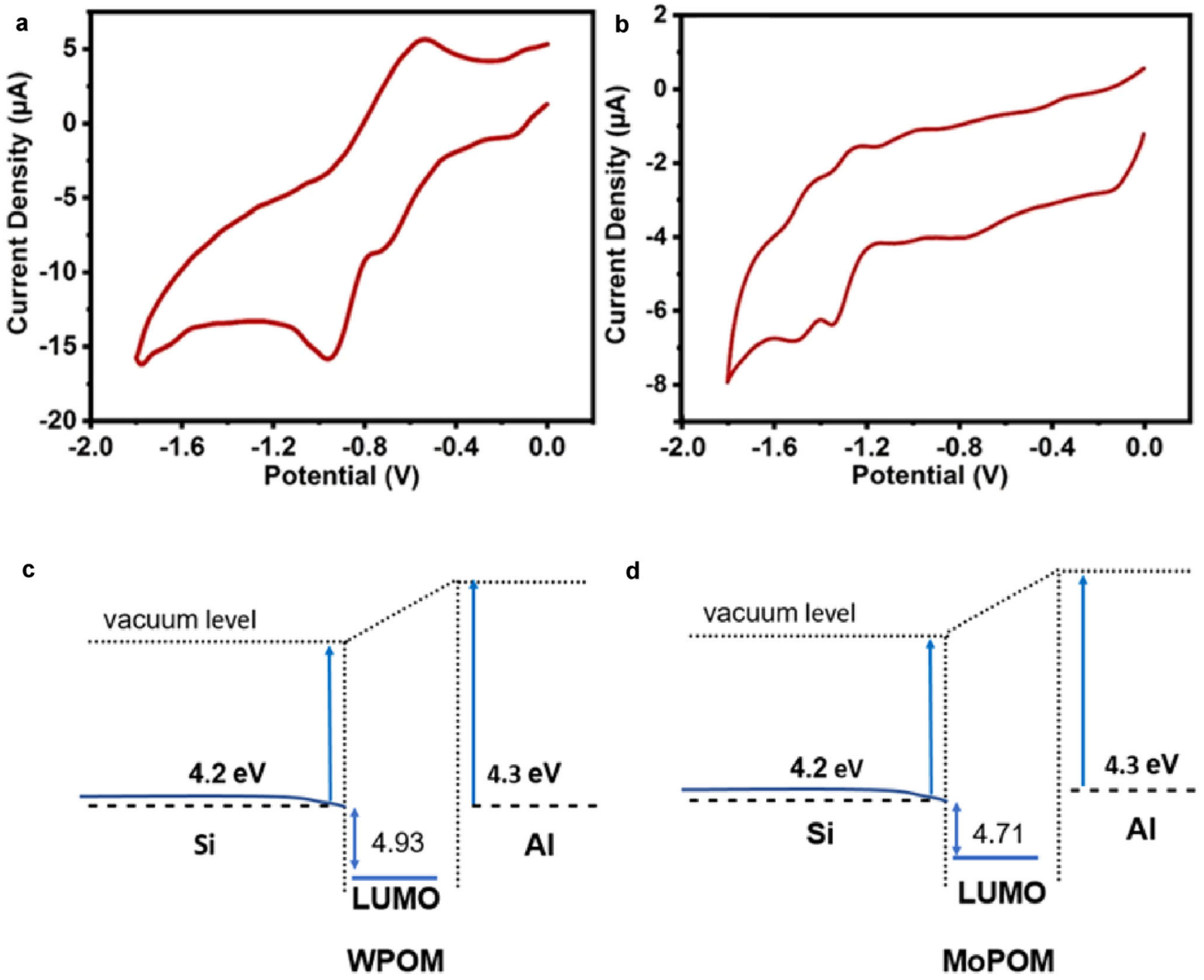

Fig. 5 Cyclic voltammogram of **a** WPOM and **b** MoPOM in 10^{-1} M Bu_4NBF_4/ACN at a scan rate of 200 mV/s, schematic energy diagram of **c** WPOM and **d** MoPOM drop as deduced from the *I–V* measurements

Table 2 Cyclic voltammetry data and LUMO energy levels of WPOM, and MOPOM compounds

Compound code	E_{red} (V)	E_{ox} (V)	LUMO (eV)
WPOM	− 0.541	− 0.136	
	− 0.471	− 0.554	− 4.931
	− 0.966	− 1.298	
MoPOM	− 0.209	− 0.362	
	− 0.765	− 0.847	− 4.710
	− 1.506	− 1.458	

To compare and better understand the electrical properties of the photodiodes, the *I–V* characteristics of the Al/*n*–Si, Al/WPOM/*n*–Si and Al/MoPOM/*n*–Si were plotted for the dark and 100 mW/cm^2 conditions together. Figure 7a and b exhibit the *I–V* characteristics of the Al/*n*–Si, Al/WPOM/*n*–Si and Al/MoPOM/*n*–Si photodiodes under dark and 100 mW/cm^2 light power illumination intensity, respectively. *I–V* characteristics of the photodiodes for dark condition revealed that the reverse or leakage current is the lowest for Al/*n*–Si reference device. The reason of the 10 times higher leakage current for POM interlayered photodiodes is due to electron acceptor behavior of the POM layers [50, 51]. This result also approves good device structure for photodiodes or photodetectors. The bending at the forward bias curve after second region shows series resistance effect or this bending is due to series resistance of these kinds of devices. The Al/*n*–Si reference device

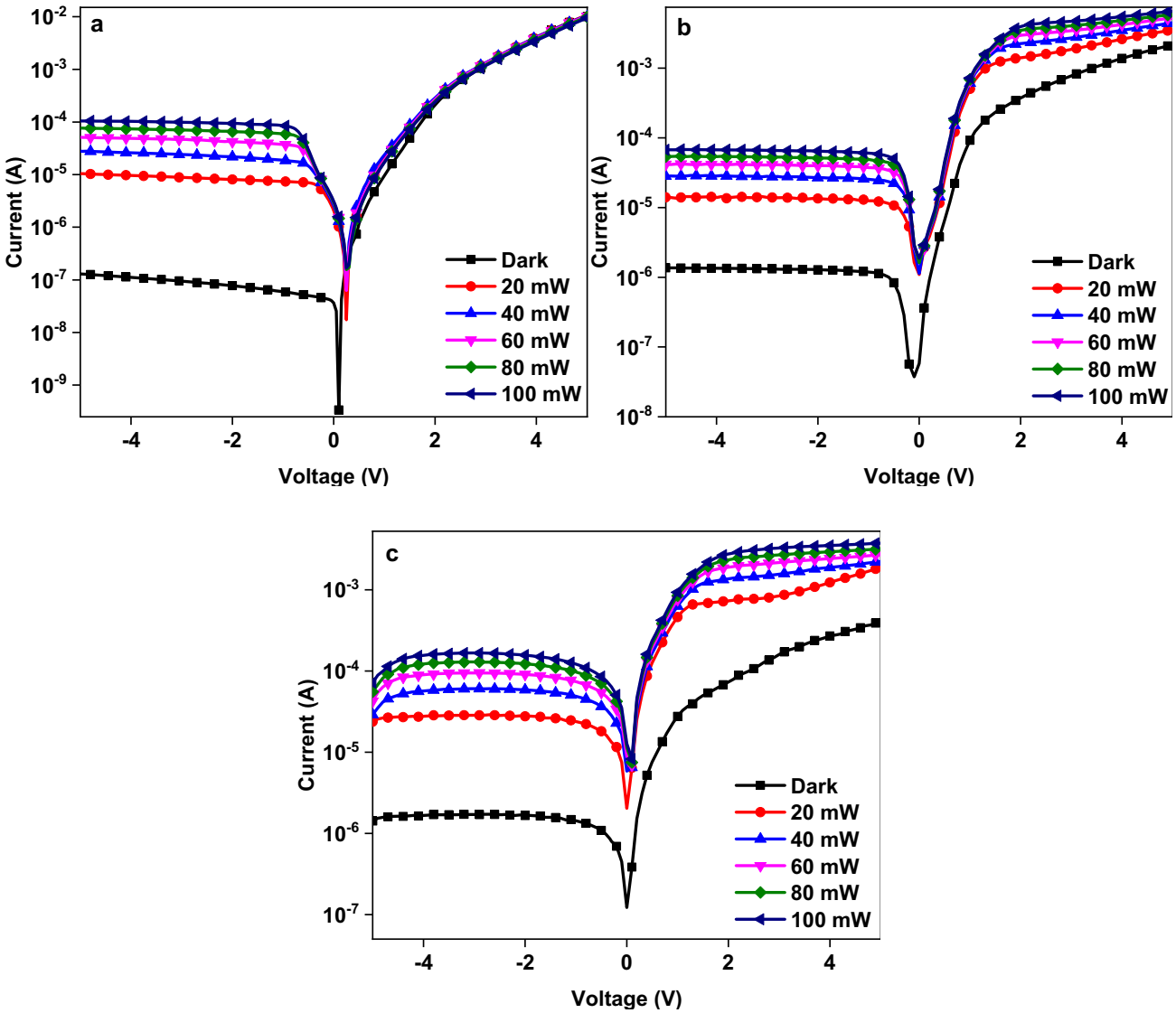

Fig. 6 The *I–V* characteristics of the **a** Al/*n*–Si (reference), **b** Al/WPOM/*n*–Si and Al/MoPOM/*n*–Si photodiodes under various illumination intensities for per cm^2 diode area

has high series resistance than POM interlayered devices according to *I–V* characteristics. In the case of 100 mW/cm^2 light power intensity condition, there are no so much changes in the leakage current or reverse current for three devices, but the forward currents increase suddenly at zero and lower forward region for POM interlayered devices. This can be attributed to again electron acceptor behavior of the POM.

The various parameters such as ideality factor (n), series resistance (R_s) as well as barrier height (ϕ_b) that characterize the photodiodes can be obtained by *I–V* measurements to understand electrical behaviors. The device parameters can be calculated by thermionic emission theory. The current (I) is obtained by following equation according to this theory:

$$I = I_0 \exp\left(\frac{qV}{nkT}\right)\left[1 - \exp\left(-\frac{qV}{nkT}\right)\right] \quad (1)$$

where I_0 is saturation current and it is given by following formula:

$$I_0 = AA^*T^2 \exp\left(-\frac{q\phi_b}{kT}\right) \quad (2)$$

where q and k exhibit charge of the electron and Boltzmann's constant. While the T represents the measurement temperature, the A and A^* display the

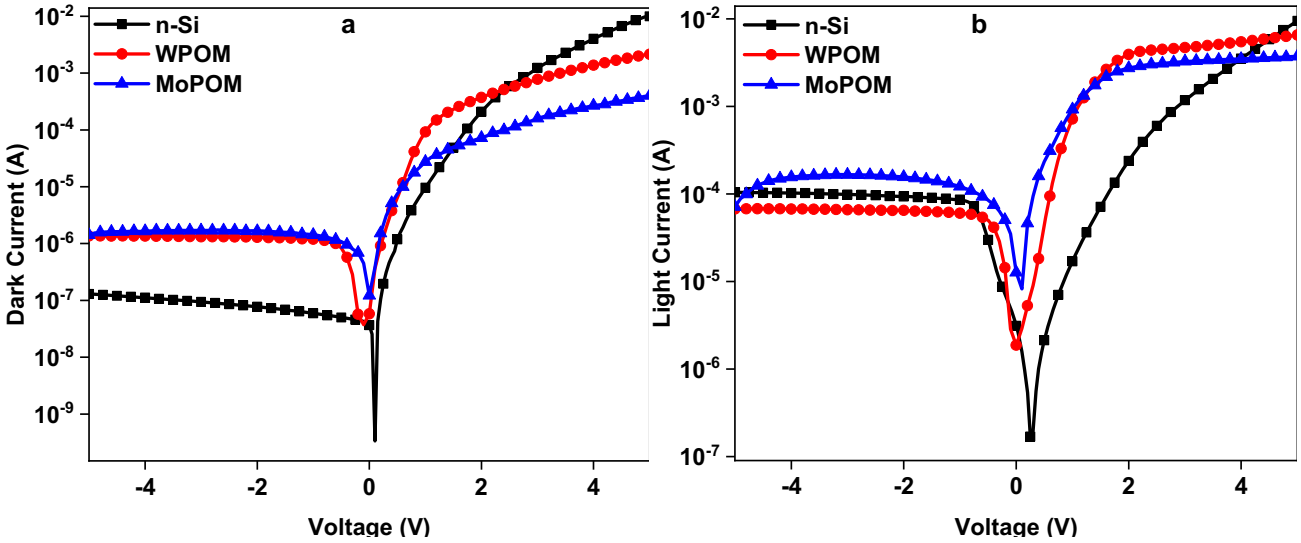

Fig. 7 The comparison the *I–V* characteristics of the Al/*n*–Si (reference), Al/WPOM/*n*–Si and Al/MoPOM/*n*–Si photodiodes a) under dark and b) under 100 mW/cm^2 light illumination intensity

diode area (in here A is equal to 7.85 × 10^{-3} cm^2) and Richardson constant (120 Acm^{-2} K^{-2} for *n*-type Si), respectively. While the ϕ_b can be calculated by the determination of the saturation current from Eq. 2, the n value for $V \geq 3kT/q$ can be obtained by the slope of the second linear region at the *I–V* curve. Thus both n and ϕ_b can be given by following formulas:

$$n = \frac{q}{kT}\left(\frac{dV}{d\ln I}\right) \tag{3}$$

$$\phi_b = \frac{kT}{q}\ln\left(\frac{A^* A T^2}{I_0}\right) \tag{4}$$

Furthermore, the rectifying ratio (*RR*) values were calculated from the $RR = I_{forward}/I_{reverse}$ formula at 3 V for the Al/*n*–Si, Al/WPOM/*n*–Si and Al/MoPOM/*n*–Si photodiodes to understand the rectifying behavior. The *RR* values were studied and discussed in the literature for various organic interlayers [52–54]. Figure 8 exhibits the *RR* changes of the Al/*n*–Si, Al/WPOM/*n*–Si and Al/MoPOM/*n*–Si photodiodes depending on the increasing light power. All devices exhibited suddenly decreasing profile with increasing light power from dark to 20 mW/cm^2 light illumination. Then, the *RR* values decreased slightly further increasing illumination intensity. The Al/*n*–Si has the highest *RR* value as 13.15 × 10^3 under dark and WPOM and MoPOM interlayered devices have *RR* values of 590.92 and 93.46. The reason for lower *RR* values with POM

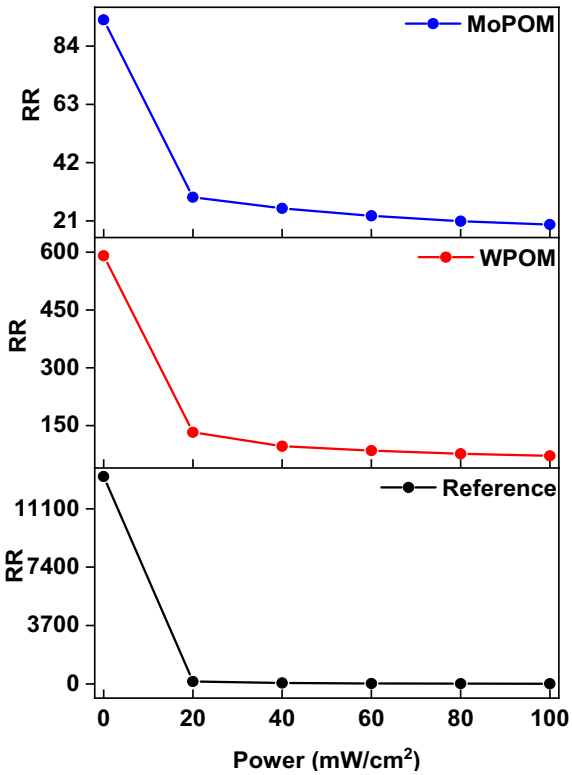

Fig. 8 The changing *RR* values of the Al/*n*–Si (reference), Al/WPOM/*n*–Si and Al/MoPOM/*n*–Si photodiodes depending on the light power intensity

interlayer can be attributed increasing leakage current.

The calculated n and ϕ_b values from above equations are listed in Table 3 for the Al/*n*–Si, Al/

Table 3 The diode parameters of the Al/WPOM/*n*–Si and Al/MoPOM/*n*–Si photodiode for various methods

Device type	Saturation current (I_0) (A)	n (I–V) –	n Cheung –	ϕ_b (I–V) (eV)	ϕ_b Cheung (eV)	ϕ_b Norde (eV)	R_s Cheung [kΩ ($H(I)$)]	R_s Cheung [(kΩ ($d\ln(I)$]	R_s Norde (kΩ)
Ref	2.78×10^{-8}	4.91	5.12	0.74	0.75	0.77	16.9	17.0	7.33
WPOM	1.31×10^{-7}	5.81	6.07	0.70	0.65	0.72	2.87	2.91	1.28
MoPOM	5.05×10^{-7}	7.29	7.30	0.67	0.65	0.68	13.5	13.6	3.55

WPOM/*n*–Si and Al/MoPOM/*n*–Si photodiodes. The Al/*n*–Si photodiode has lowest ideality factor value and highest barrier height. While the ideality factor value increased with WPOM and MoPOM interfacial layers, the barrier height vale decreased. The increase at the n and the decrease at the ϕ_b values with POM interfacial layer can be attributed to increasing interface states and charge carriers due to POM [55]. The higher n values than unity can be attributed to interface states, barrier inhomogeneity or native oxide layer for Al-nSi and interfacial POM layers for Al/WPOM/*n*–Si and Al/MoPOM/*n*–Si photodiodes [56, 57].

The junction resistance (R_j) should be studied to understand electrical performance of the photodiodes. The R_j can be obtained from *I*–*V* characteristics [58]. It has shunt resistance (R_{sh}) component owing to metal–semiconductor interface contact and series resistance (R_s) component due to interfacial layers [59]. The R_j is obtained by following equation:

$$R_j = \frac{\partial V}{\partial I} \tag{5}$$

Figure 9a–c indicate the R_j–V plots of the Al/*n*–Si, Al/WPOM/*n*–Si and Al/MoPOM/*n*–Si photodiodes, respectively. The R_{sh} and R_s values are determined from reverse bias and forward bias R_j values, respectively. All photodiodes have almost constant series resistance according to forward bias region of the R_j–V plots. However, there are differences at reverse bias or R_{sh} values by changing the photodiodes. In the case of the Al/*n*–Si reference photodiode, the R_{sh} values increased suddenly at around zero bias and reached higher values as 10^7 Ω level. In the case of POM interlayered photodiodes, the R_{sh} values increased after zero bias voltage gave a peak at around − 3 V bias. However, the R_{sh} values of the WPOM interlayered photodiode are higher than MoPOM interlayered photodiode. While the R_{sh} values of the WPOM interlayered photodiode continued to increase after the peak, the R_{sh} values of the MoPOM interlayered photodiode decreased towards zero. This kind of behavior can be attributed to POM structure.

Norde technique can be used to confirm the barrier height and series resistance calculation as another technique. The Norde function provides to calculate these parameters as given in below equation [60]:

$$F(V) = \frac{V}{\gamma} - \frac{kT}{q}\ln\left(\frac{I(V)}{AA^*T^2}\right) \tag{6}$$

where $I(V)$ is expressed voltage depended current, and γ is closest integer higher than n. The ϕ_b and R_s is calculated by next equations:

$$\phi_b = F(V_0) + \left[\frac{V_0}{\gamma} - \frac{kT}{q}\right] \tag{7}$$

$$R_s = \frac{\gamma - n}{I}\frac{kT}{q} \tag{8}$$

where V_0 exhibits the minimum voltage depending the $F(V)$. Figure 10a–c show the $F(V)$ versus V plots of the Al/*n*–Si, Al/WPOM/*n*–Si and Al/MoPOM/*n*–Si photodiodes, respectively. All plots revealed the normal Norde plots, and the calculated ϕ_b and R_s values are given in Table 3 for all devices. The γ values here were used higher integer than the n values of thermionic emission theory. The γ values were determined 5, 6 and 8 for the Al/*n*–Si, Al/WPOM/*n*–Si and Al/MoPOM/*n*–Si photodiodes, respectively. The obtained ϕ_b and R_s values are good agreement with the thermionic emission values. Small differences at the ϕ_b and R_s values can be attributed to approximation [59].

Series resistance as well as ideality factor and barrier height can be confirmed by Cheung method for only nonlinear region of forward bias *I*–*V* curve [61]. The Cheung functions are given by the following equations as $dV/d(\ln I)$ and $H(I)$:

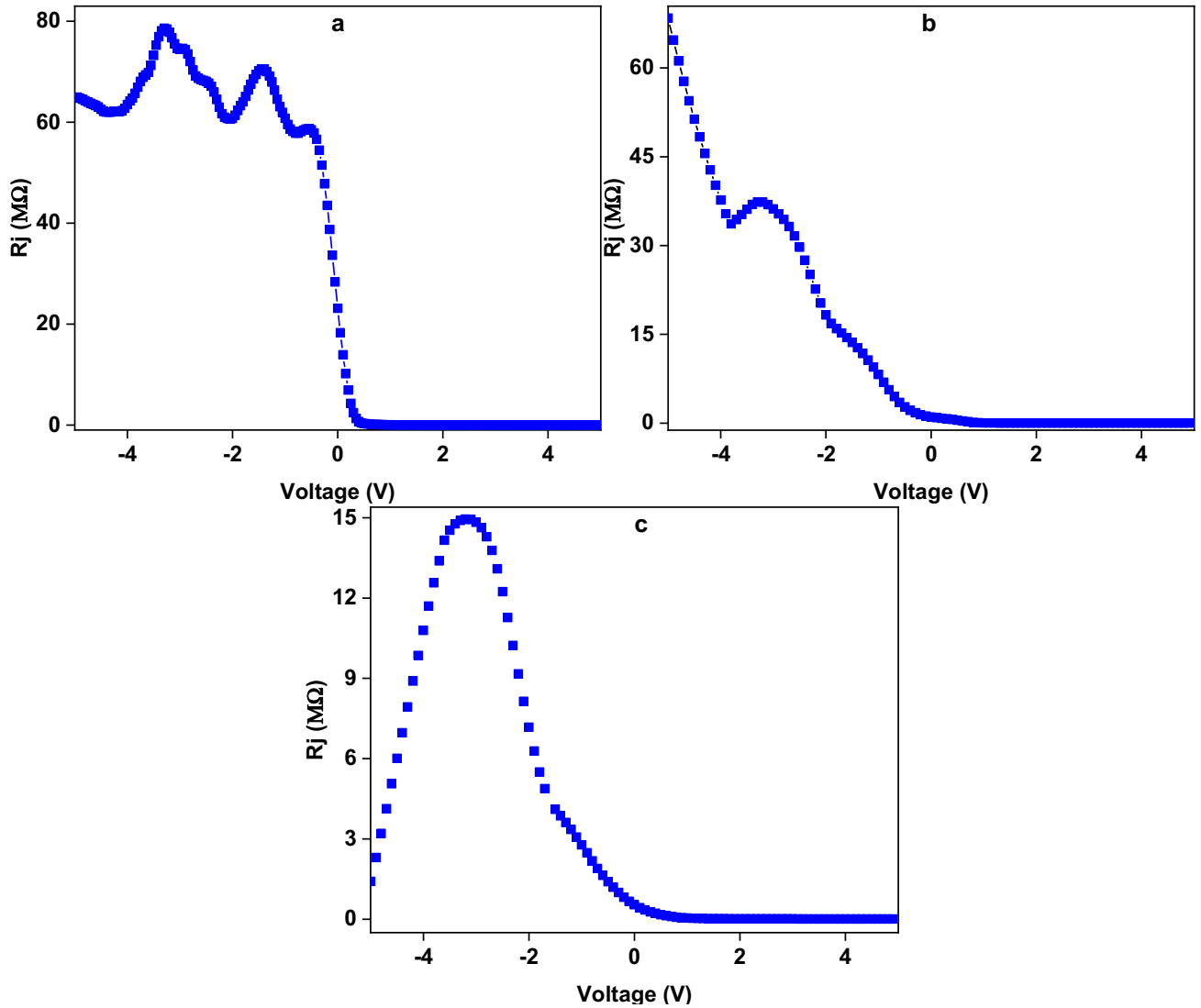

Fig. 9 The R_j-V plots of the **a** Al/n–Si (reference), **b** Al/WPOM/n–Si and **c** Al/MoPOM/n–Si photodiodes

$$\frac{dV}{d(\ln I)} = IR_s + n\frac{kT}{q} \tag{9}$$

$$H(I) = V - n\left(\frac{kT}{q}\right)\ln\left(\frac{I}{AA^*T^2}\right) \tag{10}$$

where $H(I)$ can be shortened as:

$$H(I) = IR_s + n\phi_b \tag{11}$$

According to Eqs. 9 and 11, both $dV/d(\ln I)$ and $H(I)$ functions give linear graph due to linear relation between functions and current. While the slops of the these plots give two different R_s values, the intercepts reveals the n from $dV/d(\ln I)$ and ϕ_b from $H(I)$ functions [62, 63]. The Chung plots of the Al/n–Si, Al/WPOM/n–Si and Al/MoPOM/n–Si photodiodes have been displayed in Fig. 11a–c, respectively. There are some deviations from linearity for $dV/d(\ln I)$ graphs due to the interfacial layer effect. The calculated n, ϕ_b and R_s values have been listed in Table 3 for the Al/n–Si, Al/WPOM/n–Si and Al/MoPOM/n–Si photodiodes. Firstly, the obtained series resistance values from $dV/d(\ln I)$ and $H(I)$ functions are in good agreement for each device and confirm the consistency of method. Secondly, obtained ideality factor and barrier height values from thermionic emission theory and Cehung method are in good harmony each other for all devices. The small differences between diode parameters can be attributed to approximation differences and non-ideal device structures [64, 65].

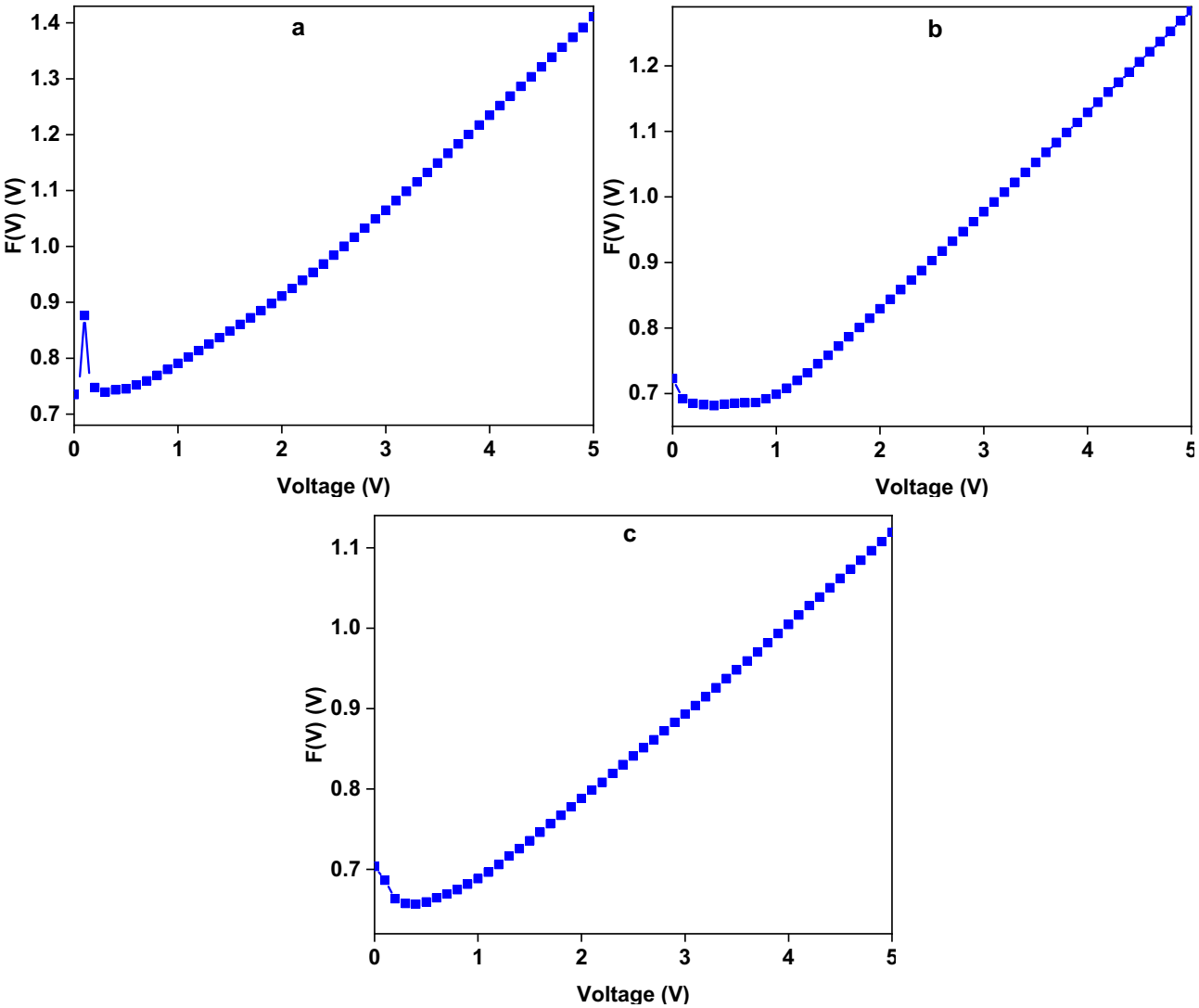

Fig. 10 The *F*(*V*)-*V* plots of the a) Al/*n*–Si (reference), b) Al/WPOM/*n*–Si and c) Al/MoPOM/*n*–Si photodiodes

The other important parameters for photodiodes or photodetectors are responsivity, photosensitivity and specific detectivity. The responsivity represents the response of the incident light, photosensitivity exhibits sensing degree of incident light, and the specific detectivity shows the detection limit of a weak signal [66–68]. Figure 12a–c display the responsivity, photosensitivity and specific detectivity of the Al/*n*–Si, Al/WPOM/*n*–Si and Al/MoPOM/*n*–Si photodiodes, respectively. The responsivity and specific detectivity values of the Al/*n*–Si and Al/WPOM/*n*–Si decreased with increasing light power, but they almost did not change for the Al/MoPOM/*n*–Si photodiode. All devices exhibited linear increasing profile with increasing light power. However, the photosensitivity slope of the Al/MoPOM/*n*–Si photodiode is the highest.

4 Conclusions

The WPOM and MoPOM compound were synthesized chemically, and they were characterized by FTI-R, NMR, AFM, SEM and electrochemically. The NMR and FT-IR results confirmed the structural properties of the POMs. The AFM and SEM images revealed the porous surface morphology of the POM structures. The WPOM and MoPOM were employed as interlayer for the Schottky type photodiode. The Al/*n*–Si (reference), Al/WPOM/*n*–Si and Al/MoPOM/*n*–Si photodiodes were fabricated by thermal evaporation

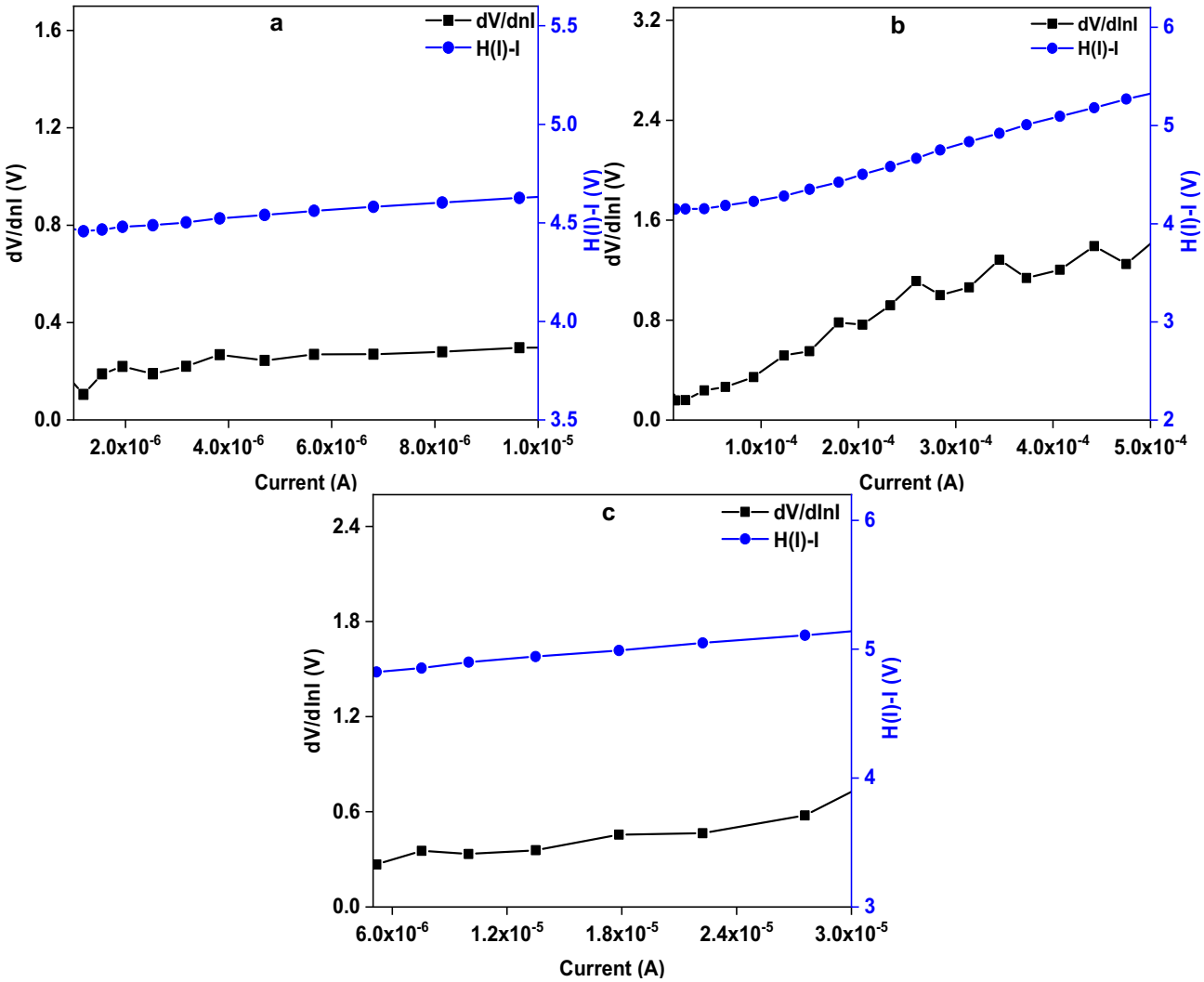

Fig. 11 The Cheung plots of the **a** Al/*n*–Si (reference), **b** Al/WPOM/*n*–Si and **c** Al/MoPOM/*n*–Si photodiodes

and spin coating techniques. The photodiodes were characterized and compared by *I*–*V* measurements under dark and various light illumination intensities. The Al/*n*–Si photodiode exhibited good rectifying property. While the Al/*n*–Si has the highest *RR* value as 13.15 × 10^3, the WPOM and MoPOM interlayered devices have *RR* values of 590.92 and 93.46 under dark. The diode parameters such as ideality factor, barrier height and series resistance values were calculated by thermionic emission theory, Norde and Cheung methods. While the ideality factor values obtained as 4.91, 5.81 and 7.29, the barrier height values were determined as 0.74 eV, 0.70 eV and 0.67 eV for the Al/*n*–Si (reference), Al/WPOM/*n*–Si and Al/MoPOM/*n*–Si photodiodes, respectively. The responsivity, photosensitivity and specific detectivity values were accounted and compared for the Al/*n*–Si, Al/WPOM/*n*–Si and Al/MoPOM/*n*–Si photodiodes with increasing light power. While the maximum responsivity and photosensitivity were obtained Al/MoPOM/*n*–Si photodiode, the maximum specific detectivity was calculated for Al/*n*–Si photodiode. Consequently, the results show that POM interlayered photodiodes and photodetectors can be used in industrial applications. Due to their excellent optical and electrochemical properties, POMs can be suggested as innovative materials for new generation perovskite solar cells and thin film devices such as thin film transistors and light emitting diodes.

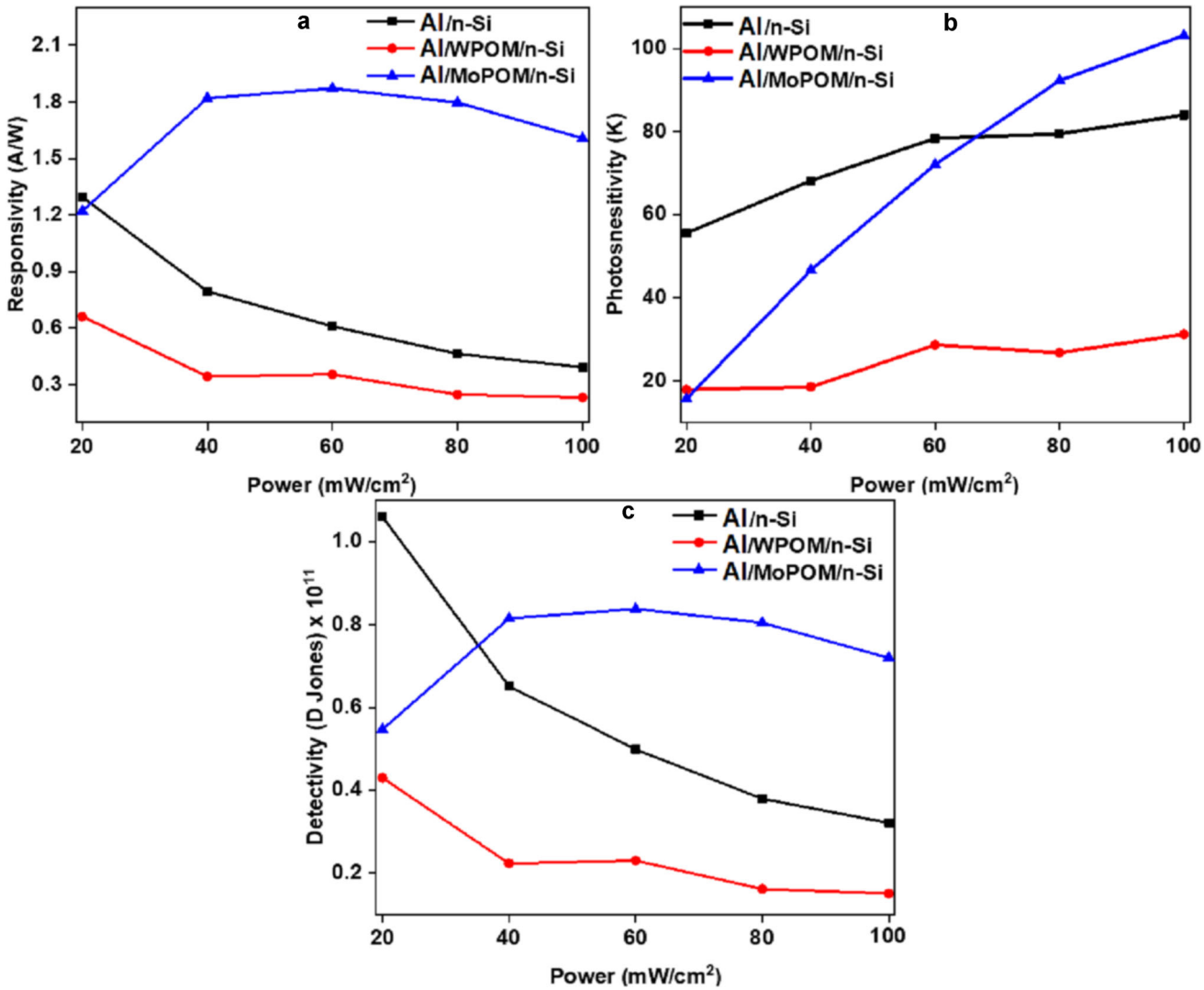

Fig. 12 **a** Responsivity, **b** photosensitivity and **c** Detectivity versus power plots of the Al/*n*–Si (reference), Al/WPOM/*n*–Si and Al/MoPOM/*n*–Si photodiodes

References

1. Y.-F. Song, R. Tsunashima, Recent advances on polyoxometalate-based molecular and composite materials. Chem. Soc. Rev. **41**, 7384 (2012). https://doi.org/10.1039/c2cs35143a
2. R. Neumann, Applications of polyoxometalates in homogeneous catalysis, in *Polyoxometalate molecular science*. (Springer, Netherlands, Dordrecht, 2003), pp. 327–349. https://doi.org/10.1007/978-94-010-0091-8_11
3. C.L. Hill, Progress and challenges in polyoxometalate-based catalysis and catalytic materials chemistry. J. Mol. Catal. A **262**, 2–6 (2007). https://doi.org/10.1016/j.molcata.2006.08.042
4. B. Hasenknopf, Polyoxometalates: introduction to a class of inorganic compounds and their biomedical applications. Front. Biosci. **10**, 275 (2005). https://doi.org/10.2741/1527
5. M. Vazylyev, D. Sloboda-Rozner, A. Haimov, G. Maayan, R. Neumann, Strategies for oxidation catalyzed by polyoxometalates at the interface of homogeneous and heterogeneous catalysis. Top. Catal. **34**, 93–99 (2005). https://doi.org/10.1007/s11244-005-3793-5
6. Y. Ji, L. Huang, J. Hu, C. Streb, Y.-F. Song, Polyoxometalate-functionalized nanocarbon materials for energy conversion, energy storage and sensor systems. Energy Environ. Sci. **8**, 776–789 (2015). https://doi.org/10.1039/C4EE03749A
7. T. Yamase, *Polyoxometalates Active against Tumors, Viruses, and Bacteria* (Springer, Berlin, 2003), pp. 65–116. https://doi.org/10.1007/978-3-642-41004-8_4

8. M. Shiddiq, D. Komijani, Y. Duan, A. Gaita-Ariño, E. Coronado, S. Hill, Enhancing coherence in molecular spin qubits via atomic clock transitions. Nature **531**, 348–351 (2016). https://doi.org/10.1038/nature16984
9. J.M. Clemente-Juan, E. Coronado, A. Gaita-Ariño, Magnetic polyoxometalates: from molecular magnetism to molecular spintronics and quantum computing. Chem. Soc. Rev. **41**, 7464 (2012). https://doi.org/10.1039/c2cs35205b
10. S. Omwoma, W. Chen, R. Tsunashima, Y.-F. Song, Recent advances on polyoxometalates intercalated layered double hydroxides: from synthetic approaches to functional material applications. Coord. Chem. Rev. **258–259**, 58–71 (2014). https://doi.org/10.1016/j.ccr.2013.08.039
11. S.-M. Wang, L. Liu, W.-L. Chen, E.-B. Wang, High performance visible and near-infrared region electrochromic smart windows based on the different structures of polyoxometalates. Electrochim. Acta **113**, 240–247 (2013). https://doi.org/10.1016/j.electacta.2013.09.048
12. A.V. Anyushin, A. Kondinski, T.N. Parac-Vogt, Hybrid polyoxometalates as post-functionalization platforms: from fundamentals to emerging applications. Chem. Soc. Rev. **49**, 382–432 (2020). https://doi.org/10.1039/C8CS00854J
13. C. Brevard, R. Schimpf, G. Tourne, C.M. Tourne, Tungsten-183 NMR: a complete and unequivocal assignment of the tungsten-tungsten connectivities in heteropolytungstates via two-dimensional tungsten-183 NMR techniques. J. Am. Chem. Soc. **105**, 7059–7063 (1983). https://doi.org/10.1021/ja00362a008
14. G.M. Brown, M.R. Noe-Spirlet, W.R. Busing, H.A. Levy, Dodecatungstophosphoric acid hexahydrate, $(H_5O_2^+)_3(PW_{12}O_{40}^{3-})$. The true structure of Keggin's 'pentahydrate' from single-crystal X-ray and neutron diffraction data. Acta Crystallogr B **33**, 1038–1046 (1977). https://doi.org/10.1107/S0567740877005330
15. P.J. Domaille, The 1- and 2-dimensional tungsten-183 and vanadium-51 NMR characterization of isopolymetalates and heteropolymetalates. J. Am. Chem. Soc. **106**, 7677–7687 (1984). https://doi.org/10.1021/ja00337a004
16. B. Dawson, The structure of the 9(18)-heteropoly anion in potassium 9(18)-tungstophosphate, $K_6(P_2W_{18}O_{62})\cdot 14H_2O$. Acta Crystallogr. **6**, 113–126 (1953). https://doi.org/10.1107/S0365110X53000466
17. R.G. Finke, M.W. Droege, P.J. Domaille, Trivacant heteropolytungstate derivatives. 3. Rational syntheses, characterization, two-dimensional tungsten-183 NMR, and properties of tungstometallophosphates P2W18M4(H2O)2O6810- and P4W30M4(H2O)2O11216- (M = cobalt, copper, zinc). Inorg. Chem. **26**, 3886–3896 (1987). https://doi.org/10.1021/ic00270a014
18. M. Tountas, Y. Topal, M. Kus, M. Ersöz, M. Fakis, P. Argitis, M. Vasilopoulou, Water-soluble lacunary polyoxometalates with excellent electron mobilities and hole blocking capabilities for high efficiency fluorescent and phosphorescent organic light emitting diodes. Adv. Funct. Mater. **26**, 2655–2665 (2016). https://doi.org/10.1002/adfm.201504832
19. M. Tountas, Y. Topal, A. Verykios, A. Soultati, A. Kaltzoglou, T.A. Papadopoulos, F. Auras, K. Seintis, M. Fakis, L.C. Palilis, D. Tsikritzis, S. Kennou, A. Fakharuddin, L. Schmidt-Mende, S. Gardelis, M. Kus, P. Falaras, D. Davazoglou, P. Argitis, M. Vasilopoulou, A silanol-functionalized polyoxometalate with excellent electron transfer mediating behavior to ZnO and TiO_2 cathode interlayers for highly efficient and extremely stable polymer solar cells. J. Mater. Chem. C **6**, 1459–1469 (2018). https://doi.org/10.1039/C7TC04960A
20. M. Tountas, Y. Topal, E. Polydorou, A. Soultati, A. Verykios, A. Kaltzoglou, T.A. Papadopoulos, F. Auras, K. Seintis, M. Fakis, L.C. Palilis, D. Tsikritzis, S. Kennou, M. Koutsoureli, G. Papaioannou, M. Ersöz, M. Kus, P. Falaras, D. Davazoglou, P. Argitis, M. Vasilopoulou, Low work function lacunary polyoxometalates as electron transport interlayers for inverted polymer solar cells of improved efficiency and stability. ACS Appl. Mater. Interfaces **9**, 22773–22787 (2017). https://doi.org/10.1021/acsami.7b04600
21. A. Kyndiah, A. Ablat, S. Guyot-Reeb, T. Schultz, F. Zu, N. Koch, P. Amsalem, S. Chiodini, T. Yilmaz Alic, Y. Topal, M. Kus, L. Hirsch, S. Fasquel, M. Abbas, A multifunctional ınterlayer for solution processed high performance ındium oxide transistors. Sci. Rep. **8**, 10946 (2018). https://doi.org/10.1038/s41598-018-29220-0
22. Q. Wang, Y. Shao, P. Gong, X. Shi, Metal-2D multilayered semiconductor junctions: layer-number dependent Fermi-level pinning. J. Mater. Chem. C **8**, 3113–3119 (2020). https://doi.org/10.1039/c9tc06331e
23. I.A. Digdaya, G.W.P. Adhyaksa, B.J. Trześniewski, E.C. Garnett, W.A. Smith, Interfacial engineering of metal-insulator-semiconductor junctions for efficient and stable photoelectrochemical water oxidation. Nat. Commun. **8**, 1–8 (2017). https://doi.org/10.1038/ncomms15968
24. M.O. Erdal, A. Kocyigit, M. Yıldırım, The rate of Cu doped TiO_2 interlayer effects on the electrical characteristics of Al/Cu:TiO_2/n-Si (MOS) capacitors depend on frequency and voltage. Microelectron. Reliab. **106**, 113591 (2020). https://doi.org/10.1016/j.microrel.2020.113591
25. H.E. Lapa, A. Kökce, A.F. Özdemir, A. Altlndal, Investigation of dielectric properties, electric modulus and conductivity of the Au/Zn-doped PVA/n-4H-SiC (MPS) structure using impedance spectroscopy method. Z. Fur Phys. Chem. (2019). https://doi.org/10.1515/zpch-2017-1091

26. Ö. Sevgili, Y. Azizian-Kalandaragh, Ş Altındal, Frequency and voltage dependence of electrical and dielectric properties in metal-interfacial layer-semiconductor (MIS) type structures. Phys. B **587**, 412122 (2020). https://doi.org/10.1016/j.physb.2020.412122
27. A. Kocyigit, M. Yilmaz, S. Aydogan, U. Incekara, Y. Sahin, The performance of chitosan layer in Au/n-Si sandwich structures as a barrier modifier. Polym. Test. **89**, 106546 (2020). https://doi.org/10.1016/j.polymertesting.2020.106546
28. R. Contant, Relations entre les tungstophosphates apparentés à l'anion PW12O403−. Synthèse et propriétés d'un nouveau polyoxotungstophosphate lacunaire K10P2W20O70·24H2O. Can. J. Chem. **65**, 568–573 (1987). https://doi.org/10.1139/v87-100
29. G. Turgut, S. Aydogan, M. Yilmaz, A. Özmen, H. Kacus, An investigation of spray deposited CdO films and CdO/p-Si heterojunction at different substrate temperatures. JOM **73**, 566–573 (2021). https://doi.org/10.1007/s11837-020-04514-9
30. A. Özmen, S. Aydogan, M. Yilmaz, Fabrication of spray derived nanostructured n-ZnO/p-Si heterojunction diode and investigation of its response to dark and light. Ceram. Int. (2019). https://doi.org/10.1016/j.ceramint.2019.04.210
31. M. Guzel, Y. Torlak, E. Karatas, M. Ak, Optical and electrical properties of monolacunary keggin-type polyoxometalate/star-shaped polycarbazole nanocomposite film. J. Electrochem. Soc. **166**, H313–H319 (2019). https://doi.org/10.1149/2.0531908jes
32. J. Niu, M. Li, J. Wang, Organosilyl derivatives of trivacant tungstophosphate of general formula α-A-[PW9O34(R-SiO)3(RSi)]3−. J. Organomet. Chem. **675**, 84–90 (2003). https://doi.org/10.1016/S0022-328X(03)00252-3
33. Y. Huang, X. Duan, Q. Wei, C.M. Lieber, Directed assembly of one-dimensional nanostructures into functional networks. Science (2001). https://doi.org/10.1126/science.291.5504.630
34. A.S. Cherevan, S.P. Nandan, I. Roger, R. Liu, C. Streb, D. Eder, Polyoxometalates on functional substrates: concepts, synergies, and future perspectives. Adv. Sci. **7**, 1903511 (2020). https://doi.org/10.1002/advs.201903511
35. M. Raula, G. Ganor, M. Saganovich, O. Zeiri, Y. Wang, M.R. Chierotti, R. Gobetto, I.A. Weinstock, Polyoxometalate complexes of anatase-titanium dioxide cores in water. Angew. Chem. - Int. Ed. **54**, 12416–12421 (2015). https://doi.org/10.1002/anie.201501941
36. M. Ishaque Khan, L.S. Swenson, Open-framework hybrid materials and composites from polyoxometalates, in *New future developments in catalalysis. Hybrid Materials Composites Organocatalysts*. (Elsevier, Amsterdam, 2013), pp. 27–54
37. A. Hiskia, A. Mylonas, E. Papaconstantinou, Comparison of the photoredox properties of polyoxometallates and semiconducting particles. Chem. Soc. Rev. **30**, 62–69 (2001). https://doi.org/10.1039/a905675k
38. P. Kormali, A. Troupis, T. Triantis, A. Hiskia, E. Papaconstantinou, Photocatalysis by polyoxometallates and TiO_2: a comparative study. Catal. Today **124**, 149–155 (2007). https://doi.org/10.1016/j.cattod.2007.03.032
39. A. Proust, R. Thouvenot, P. Gouzerh, Functionalization of polyoxometalates: towards advanced applications in catalysis and materials science. Chem. Commun. (2008). https://doi.org/10.1039/b715502f
40. D. Agustin, C. Coelho, A. Mazeaud, P. Herson, A. Proust, R. Thouvenot, Organic-inorganic hybrids based on polyoxometalates. Part 8. Synthesis and spectroscopic characterization of the heterosilylated anions [PW(9)O(34)((t)BuSiO)(3)(SiR)](3-) (R = -CH(3), -CH=CH(2), -CH(2)-CH=CH(2), -(Ci(2))(4)-CH=CH(2)) - X-ray crystal stru. Z. Fur Anorg. Und Allg. Chem. (2004). https://doi.org/10.1002/zaac.200400276
41. J. Niu, M. Li, J. Wang, Organosilyl derivatives of trivacant tungstophosphate of general formula α-A-[PW9O34(RSiO)3(RSi)]3-: synthesis and structure determination by X-ray crystallography. J. Organomet. Chem. (2003). https://doi.org/10.1016/S0022-328X(03)00252-3
42. D. Agustin, J. Dallery, C. Coelho, A. Proust, R. Thouvenot, Synthesis, characterization and study of the chromogenic properties of the hybrid polyoxometalates [PW11O39(-SiR)2O]3- (R = Et, (CH2)nCH{double bond, long}CH2 (n = 0, 1, 4), CH2CH2SiEt3, CH2CH2SiMe2Ph). J. Organomet. Chem. (2007). https://doi.org/10.1016/j.jorganchem.2006.10.027
43. T.M. Anderson, W.A. Neiwert, M.L. Kirk, P.M.B. Piccoli, A.J. Schultz, T.F. Koetzle, D.G. Musaev, K. Morokuma, R. Cao, C.L. Hill, A late-transition metal oxo complex: K7Na9[O=Pt IV(H2O)L2], L = [PW9O 34]9-. Science (2004). https://doi.org/10.1126/science.1104696
44. R. Ayranci, Y. Torlak, T. Soganci, M. Ak, Trilacunary Keggin type polyoxometalate-conducting polymer composites for amperometric glucose detection. J. Electrochem. Soc. **165**, B638–B643 (2018). https://doi.org/10.1149/2.1061813jes
45. C.J. Wu, G.J. Wang, C.H. Kao, Z.J. Yang, H. Chen, Y. Sen Lin, C.F. Lin, J. Han, Photon-recycling in ultraviolet GaN-based photodiodes with porous AlGaN distributed bragg reflectors. ACS Appl. Nano Mater. **2**, 5044–5048 (2019). https://doi.org/10.1021/acsanm.9b00973
46. J. Kim, S.S. Joo, K.W. Lee, J.H. Kim, D.H. Shin, S. Kim, S.H. Choi, Near-ultraviolet-sensitive graphene/porous silicon photodetectors. ACS Appl. Mater. Interfaces **6**, 20880–20886 (2014). https://doi.org/10.1021/am5053812
47. M. Laurans, K. Dalla Francesca, F. Volatron, G. Izzet, D. Guerin, D. Vuillaume, S. Lenfant, A. Proust, Molecular

signature of polyoxometalates in electron transport of silicon-based molecular junctions. Nanoscale **10**, 17156–17165 (2018). https://doi.org/10.1039/C8NR04946G

48. T. Ye, J. Wang, G. Dong, Y. Jiang, C. Feng, Y. Yang, Recent progress in the application of polyoxometalates for dye-sensitized/organic solar cells. Chin. J. Chem. **34**, 747–756 (2016). https://doi.org/10.1002/cjoc.201600231
49. H.H. Gullu, D.E. Yildiz, A. Kocyigit, M. Yıldırım, Electrical properties of Al/PCBM:ZnO/p-Si heterojunction for photodiode application. J. Alloys Compd. **827**, 154279 (2020). https://doi.org/10.1016/j.jallcom.2020.154279
50. H. Zhang, T. Wang, W. Chen, Polyoxometalate modified all-weather solar cells for energy harvesting. Electrochim. Acta **330**, 135215 (2020). https://doi.org/10.1016/j.electacta.2019.135215
51. D.E. Yıldız, D.H. Apaydın, L. Toppare, A. Cirpan, Effect of layer thickness on the electrical parameters and conduction mechanisms of conjugated polymer-based heterojunction diode. J. Appl. Polym. Sci. (2017). https://doi.org/10.1002/app.44817
52. M. Özer, D.E. Yıldız, Ş Altındal, M.M. Bülbül, Temperature dependence of characteristic parameters of the Au/SnO2/n-Si (MIS) Schottky diodes. Solid State Electron. **51**, 941–949 (2007). https://doi.org/10.1016/J.SSE.2007.04.013
53. H.H. Gullu, D.E. Yildiz, L. Toppare, A. Cirpan, Electrical characteristics of organic heterojunction with an alternating benzotriazole and fluorene containing copolymer. J. Mater. Sci. Mater. Electron. **31**, 18816–18831 (2020). https://doi.org/10.1007/s10854-020-04421-4
54. D.E. Yıldız, H.H. Gullu, L. Toppare, A. Cirpan, Analysis of temperature-dependent forward and leakage conduction mechanisms in organic thin film heterojunction diode with fluorine-based PCBM blend. J. Mater. Sci. Mater. Electron. **31**, 15233–15242 (2020). https://doi.org/10.1007/s10854-020-04088-x
55. A. Kocyigit, İ Karteri, I. Orak, S. Uruş, M. Çaylar, The structural and electrical characterization of Al/GO-SiO_2/p-Si photodiode. Phys. E. **103**, 452–458 (2018). https://doi.org/10.1016/j.physe.2018.06.006
56. H.H. Gullu, D.E. Yildiz, Analysis of forward and reverse biased current–voltage characteristics of Al/Al_2O_3/n-Si Schottky diode with atomic layer deposited Al_2O_3 thin film interlayer. J. Mater. Sci. Mater. Electron. **30**, 19383–19393 (2019). https://doi.org/10.1007/s10854-019-02300-1
57. D.E. Yildiz, Ş Altindal, Z. Tekeli, M. Özer, The effects of surface states and series resistance on the performance of Au/SnO_2/n-Si and Al/SnO_2/p-Si (MIS) Schottky barrier diodes. Mater. Sci. Semicond. Process. **13**, 34–40 (2010). https://doi.org/10.1016/j.mssp.2010.02.004
58. L.D. Rao, V.R. Reddy, Electrical parameters and series resistance analysis of Au/Y/p-InP/Pt Schottky barrier diode at room temperature, in *AIP conference proceedings*. (AIP Publishing LLC, College Park, 2016), p. 120020. https://doi.org/10.1063/1.4948092
59. M. Yilmaz, A. Kocyigit, B.B. Cirak, H. Kacus, U. Incekara, S. Aydogan, The comparison of Co/hematoxylin/n-Si and Co/hematoxylin/p-Si devices as rectifier for a wide range temperature. Mater. Sci. Semicond. Process. **113**, 105039 (2020). https://doi.org/10.1016/j.mssp.2020.105039
60. H. Norde, A modified forward I-V plot for Schottky diodes with high series resistance. J. Appl. Phys. **50**, 5052–5053 (1979). https://doi.org/10.1063/1.325607
61. S.K. Cheung, N.W. Cheung, Extraction of Schottky diode parameters from forward current-voltage characteristics. Appl. Phys. Lett. **49**, 85 (1986). https://doi.org/10.1063/1.97359
62. Ş Karataş, Effect of series resistance on the electrical characteristics and interface state energy distributions of Sn/p-Si (MS) Schottky diodes. Microelectron. Eng. **87**, 1935–1940 (2010). https://doi.org/10.1016/j.mee.2009.11.168
63. A. Kocyigit, İ Orak, The electrical characterization effect of insulator layer between semiconductor and metal. J. Inst. Sci. Technol. **6**, 57–67 (2016). https://doi.org/10.21597/jist.2016321840
64. D.E. Yıldız, Electrical properties of Au–Cu/ZnO/p-Si diode fabricated by atomic layer deposition. J. Mater. Sci. Mater. Electron. **29**, 17802–17808 (2018). https://doi.org/10.1007/s10854-018-9889-z
65. A. Tataroğlu, Ş Altındal, Y. Azizian-Kalandaragh, Comparison of electrical properties of MS and MPS type diode in respect of (In_2O_3-PVP) interlayer. Phys. B **576**, 411733 (2020). https://doi.org/10.1016/j.physb.2019.411733
66. O. Dayan, A. Gencer Imer, A.G. Al-Sehemi, N. Özdemir, A. Dere, Z. Şerbetçi, A.A. Al-Ghamdi, F. Yakuphanoglu, Photoresponsivity and photodetectivity properties of copper complex-based photodiode. J. Mol. Struct. **1200**, 127062 (2020). https://doi.org/10.1016/j.molstruc.2019.127062
67. Ö.B. Sürücü, H.H. Güllü, M. Terlemezoglu, D.E. Yildiz, M. Parlak, Determination of current transport characteristics in Au-Cu/CuO/n-Si Schottky diodes. Phys. B **570**, 246–253 (2019). https://doi.org/10.1016/j.physb.2019.06.024
68. H.H. Gullu, D.E. Yildiz, Ö. Bayrakli Sürücü, M. Terlemezoglu, M. Parlak, Temperature dependence of electrical properties in In/$Cu_2ZnSnTe_4$/Si/Ag diodes. Bull. Mater. Sci. **42**, 45 (2019). https://doi.org/10.1007/s12034-018-1713-0